Catalysis Science & Technology

ROYAL SOCIETY OF CHEMISTRY

PAPER

View Article Online
View Journal | View Issue

Cite this: *Catal. Sci. Technol.*, 2023, **13**, 1755

Photothermal steam reforming of methane over silica-supported nickel catalysts with temperature gradients†

Wirya Sarwana, [ab] Daichi Takami,[a] Akira Yamamoto [*ac] and Hisao Yoshida [ac]

Photothermal steam reforming of methane (PTSRM) is a promising catalytic technology for converting stable methane and water into hydrogen utilizing solar energy. In the present study, the photothermal catalytic activity of silica-supported nickel (Ni/SiO_2) catalysts was investigated using a gas-flow reactor under concentrated visible/near-infrared light irradiation with various experimental parameters to obtain insight into factors affecting the activity and selectivity. In the thermal SRM at 773 K in the dark, the CH_4 conversion reached near-equilibrium with all four Ni/SiO_2 catalysts, while there was a significant difference in activity between the catalysts in the PTSRM reaction under light irradiation. These results indicate that PTSRM activity was affected by both thermodynamic and kinetic aspects. The conversion–selectivity relationship revealed that the product selectivity in PTSRM was different from the values in thermal SRM in the dark and calculated thermodynamic equilibrium. We proposed that concentrated light irradiation created the highest temperature zone in the centre of the reactor and the lower temperature zone downstream, and the consecutive water gas shift reaction and CO hydrogenation occurred in the lower temperature zone, thus resulting in the characteristic product selectivity. This study shows the potential of PTSRM systems with controllable selectivity by the temperature gradients formed under concentrated sunlight irradiation.

Received 3rd October 2022,
Accepted 11th January 2023

DOI: 10.1039/d2cy01721k

rsc.li/catalysis

Introduction

Steam reforming of methane (SRM, eqn (1)) is one of the most established catalytic technologies in the industry for the production of hydrogen and/or carbon monoxide from methane and water.[1–6] In the commercial process, the obtained CO gas can be converted into CO_2 *via* a water gas shift (WGS, eqn (2)) reaction to obtain a high H_2 yield.

$$CH_4 + H_2O \rightarrow CO + 3H_2 \quad \Delta H^\circ = 206\ \text{kJ mol}^{-1} \qquad (1)$$

$$CO + H_2O \rightarrow CO_2 + H_2 \quad \Delta H^\circ = -41\ \text{kJ mol}^{-1} \qquad (2)$$

The overall chemical equation for producing a mixture of H_2 and CO_2 is as follows:

$$CH_4 + 2H_2O \rightarrow CO_2 + 4H_2 \quad \Delta H^\circ = 165\ \text{kJ mol}^{-1} \qquad (3)$$

SRM is a highly endothermic reaction; thus, it needs high temperatures (>973 K) to obtain sufficient conversion due to the thermodynamic limit.[7–10] To gain such high temperatures, the tremendous input of heat energy is supplied typically by methane combustion.[11,12] Considering methane as a hydrogen source, utilizing methane as a heat source lowers the H_2 yield, which is unfavourable energetically and economically. Therefore, a renewable energy source that does not consume the reactant is highly desirable for performing the SRM reaction.

Solar energy is one of the promising alternatives for SRM as an abundant and environmentally friendly energy source. For the utilization of solar energy for catalytic reaction systems, approaches are divided into three categories: photothermal[13–18] and photocatalytic systems[19–32] and their combination.[25,33] Systems using photocatalysts have been investigated extensively and attracting attention, where photogenerated electrons and holes promote the reaction. However, it is still a significant challenge to improve the quantum efficiency and develop a system that works under visible and near-infrared (vis/NIR) light, a large portion of sunlight. In contrast, photothermal SRM (PTSRM) uses concentrated solar light to raise the temperature of the catalytic zone through photothermal conversion.[17,18]

For photothermal conversion catalysts, both light absorption and catalytic properties are essential to achieve a

[a] *Graduate School of Human and Environmental Studies, Kyoto University, Kyoto 606-8501, Japan. E-mail: yamamoto.akira.2a@kyoto-u.ac.jp*
[b] *Department of Mechanical Engineering, Sumbawa University of Technology, Olat Maras, Sumbawa, West Nusa Tenggara, 84371, Indonesia*
[c] *Elements Strategy Initiative for Catalysts and Batteries (ESICB), Kyoto University, Kyoto 615-8520, Japan*

† Electronic supplementary information (ESI) available. See DOI: **https://doi.org/10.1039/d2cy01721k**

highly-active system. It is known that the incorporation of metal nanoparticles into support materials without having light absorption increased the vis/NIR absorption drastically,[34–36] and metal nanoparticles also function as catalytic active sites. Among various metals, Ni is one of the most active components for SRM and used for industrial processes. Recently, the fabrication of small and uniform Ni nanoparticles *via* the decomposition of Ni phyllosilicates (Ni PSs) has been reported as an effective method for enhancing catalytic activity in thermal SRM (TSRM).[37–39] Thus, this catalyst preparation technique would be effective in developing highly-active catalysts for PTSRM. Moreover, the photothermal catalytic system provides inhomogeneous temperature distribution under concentrated light irradiation, and the temperature gradient affects the catalytic activity. Recently, Mao *et al.* reported that the different temperature zones on the Fe catalyst and $TiO_{2-x}H_y$ under light irradiation enhanced ammonia production rates beyond the equilibrium conversion.[40] Li *et al.* reported that the thermal gradients in Ru–Cs/MgO catalysts improved the reaction rates and conversion for ammonia production under solar light irradiation.[41] Nevertheless, to the best of our knowledge, the effect of the temperature gradient in the catalyst on the catalytic performance in PTSRM has not been investigated so far.

In the present study, we fabricated four Ni/SiO_2 catalysts by decomposition of Ni PSs and impregnation with three Ni precursors, and compared their catalytic performance in PTSRM. Moreover, we investigated the effect of light conditions (*i.e.*, the power and spot size) on the catalytic performance. By comparing the product selectivity in PTSRM with the experimental and theoretical values in TSRM, we proposed that the observed temperature gradient under the catalytic reaction conditions contributes to changing the product selectivity.

Experimental

Catalyst preparation

The 20 wt% Ni/SiO_2 sample *via* Ni PS decomposition was prepared by an impregnation method using an ammonia solution.[42–45] The SiO_2 powder (Sciqas, 0.05 μm, Sakai Chemical, 2 g) was dispersed in a 28% ammonia solution (100 ml) containing nickel basic carbonate tetrahydrate ($NiCO_3{\cdot}2Ni(OH)_2{\cdot}4H_2O$, Wako, 98%) and the suspension was magnetically stirred in a water bath at 353 K until dried. The mixture was then kept in an oven at 353 K overnight. The obtained powder was mixed in an alumina mortar for 10 min and calcined at 723 K for 2 h. Before the characterization, the sample was reduced with a 10% H_2/Ar gas for 30 min (referred to as Ni-Car). The other three 20 wt% Ni/SiO_2 samples were prepared by a typical impregnation method with nickel precursors of nickel acetate tetrahydrate ($Ni(CH_3CO_2)_2{\cdot}4H_2O$, Wako, 98%), nickel nitrate hexahydrate ($Ni(NO_3)_2{\cdot}6H_2O$, Wako, 98%), and nickel lactate tetrahydrate ($Ni(C_3H_5O_3)_2{\cdot}4H_2O$, Wako, 99%) using deionized water as a solvent. These samples are referred to as Ni-Ace, Ni-Nit, and Ni-Lac, respectively.

Characterization

The X-ray diffraction (XRD) patterns were recorded on a Shimadzu Lab X XRD-6000 at room temperature using Cu Kα radiation (40 kV, 30 mA). The Ni crystallite size (d_{XRD}) was estimated from a full width at half maximum (FWHM) of the diffraction line at $2\theta = 44°$ in the XRD pattern by the Scherrer equation. The transmission electron microscopy (TEM) images were captured using a JEOL JEM-2100F at 200 kV. The dispersion of Ni (D) was calculated from the distributions of the Ni particle size by TEM using a cuboctahedral model. Ni K-edge XAFS measurements were performed at BL9A of the Photon Factory (KEK-PF, Tsukuba, Japan). The samples after the reduction treatment with a 10% H_2/Ar gas were packed using a polyethylene bag without exposure to air and measured in a transmission mode. The diffuse reflectance (DR) UV/vis/NIR spectra of the samples were measured using a JASCO V-570 equipped with an integrating sphere, where $BaSO_4$ was used as a reference. The specific surface area (S_a) was measured by N_2 adsorption at 77 K (BET method) with a Quantachrome Monosorb MS-21.

Catalytic activity test in PTSRM and TSRM

Catalytic activity tests in PTSRM and TSRM were performed using a continuous flow fixed bed reactor, as depicted in Fig. S1.† The sample powder was pressed into a pellet under 40 MPa for 1 min using a Newton press and then pulverised using an alumina mortar. The obtained granules (50–100 mesh) were added to a quartz reactor ($20 \times 20 \times 1$ mm^3). Before the activity test, the sample was pretreated with a 10% H_2/Ar gas at 873 K for 30 min using an electrical muffle furnace. Then, the reaction gas, 8% CH_4/12% H_2O/6% N_2/Ar (balance), was fed into the reactor, where the N_2 gas was used as the internal standard for quantifying the reactants and products. The partial pressure of steam was controlled by changing the temperature in the water supply. For the photothermal catalytic activity test, a 300 W Xe lamp (PE300BUV, Excelitas technologies) equipped with a cut-off filter ($\lambda > 420$ nm, W-Y435, HOYA) and a convex lens was used as the light source. The diameter of the irradiation area ($Ø$) was varied from 2.0 to 1.4 cm (typically 2.0 cm) by changing the position between the Xe lamp and reactor. The light power (P, typically 23.8 W, which corresponds to 5.95 W cm^{-2}) was controlled by changing the current values of the power supply. The maximum surface temperatures on the front ($T_{max,f}$) and back ($T_{max,b}$) sides of the reactor were measured with a radiation thermometer (TMHX-CGE2400-0150H2.2, Japan Sensor, detection wavelength: 5.0–5.6 μm, spot size: 2.2 mm). The gaseous products (5 mL) were analysed by online gas chromatography equipped with a thermal conductivity detector (GC-8A, Shimadzu) at 20 minute intervals. The CH_4 conversion, carbon balance, and

CO_2 selectivity were calculated based on the following equations:

$$CH_4 \text{ conversion } (\%) = ([CH_4]_{in} - [CH_4]_{out})/[CH_4]_{in} \times 100 \quad (4)$$

$$\text{Carbon balance} = ([CO]_{out} + [CO_2]_{out} + [CH_4]_{out})/[CH_4]_{in} \quad (5)$$

$$CO_2 \text{ selectivity } (\%) = [CO_2]_{out}/([CO_2]_{out} + [CO]_{out}) \times 100 \quad (6)$$

where $[X]_{in}$ and $[X]_{out}$ are concentrations of X (X = CH_4, CO, or CO_2) in the inlet and outlet gases, respectively. The light to chemical conversion efficiency (η) was calculated by the following equation:[35,46]

$$\eta(\%) = (r_{H_2}\Delta H^{\circ}_{CH_2} + r_{CO}\Delta H^{\circ}_{CO} - r_{CH_4}\Delta H^{\circ}_{CH_4})/P \times 100 \quad (7)$$

where, ΔH°_{CX} and r_X are the enthalpy of combustion, production rate and conversion rate of X, respectively. The thermodynamic equilibrium conversion was calculated using the NASA-CEA program.[47]

Results and discussion

Characterization of catalysts

In the Ni-Car sample, Ni PSs and Ni hydroxide were formed after the impregnation using an aqueous ammonia solution, and the Ni hydroxide was converted to Ni oxide after the calcination treatment at 723 K based on the TEM images and XRD patterns (Fig. S2†). After the H_2 reduction at 873 K, the Ni species were reduced to Ni metal, as shown in Fig. 1A, which was consistent with the previous reports.[42–45] In all the Ni samples prepared with different Ni precursors using water as a solvent, metallic Ni was observed, and there was no diffraction peak derived from impurities. Fig. 1B shows the Ni K-edge XANES spectra of the Ni/SiO_2 samples reduced at 873 K for 30 min. The shapes of the XANES spectra of the reduced Ni samples were almost identical to that of Ni foil, which indicates that all the Ni species were reduced to Ni metal after the reduction pretreatment.

The size and morphology of Ni particles in the Ni/SiO_2 samples were confirmed by TEM (Fig. 2). In the Ni-Car sample (Fig. 2A), aggregated small Ni particles were observed in a high magnification image (Fig. S3†), which was completely different from the other Ni/SiO_2 samples prepared by the conventional impregnation method. In the HAADF-STEM image of the Ni-Car sample, a contrast was observed between bright nanoparticles and a thin layer surrounding the particle (Fig. S4†), which indicates that Ni nanoparticles are partially covered by a silica shell.[42,43] Besides, the Ni-Car sample exhibited the highest S_a, followed by the Ni-Nit, Ni-Ace and Ni-Lac samples (Table 1). The increased S_a in Ni-Car would be originated from the formation and decomposition of Ni PSs and Ni nanoparticles partially covered by the SiO_2 layer.

The mean Ni particle size (d_{TEM}) by TEM in the Ni-Car sample was the smallest (7.8 nm) among the four Ni/SiO_2 samples (Ni-Ace 10.0 nm; Ni-Nit: 14.6 nm; Ni-Lac: 8.5 nm), as shown in Table 1. The crystallite size estimated from the XRD peaks using the Scherrer equation showed different values from d_{TEM}, which would be due to the relatively large particle size distribution of the Ni particles (see ESI† and Table S1).[48] The Ni dispersion was calculated from the particle size distributions by TEM (Table 1), and the order was consistent with the crystallite size by XRD.

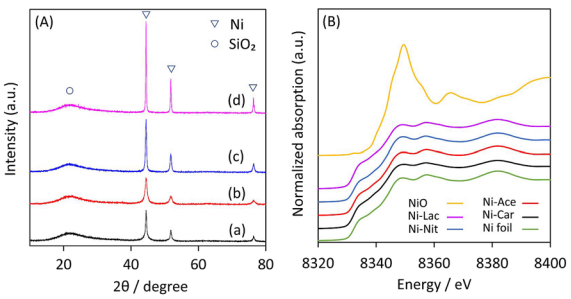

Fig. 1 XRD patterns (A) and XANES spectra (B) of the Ni/SiO_2 samples after the reduction pretreatment at 873 K. (a): Ni-Car, (b): Ni-Ace, (c): Ni-Nit, and (d): Ni-Lac.

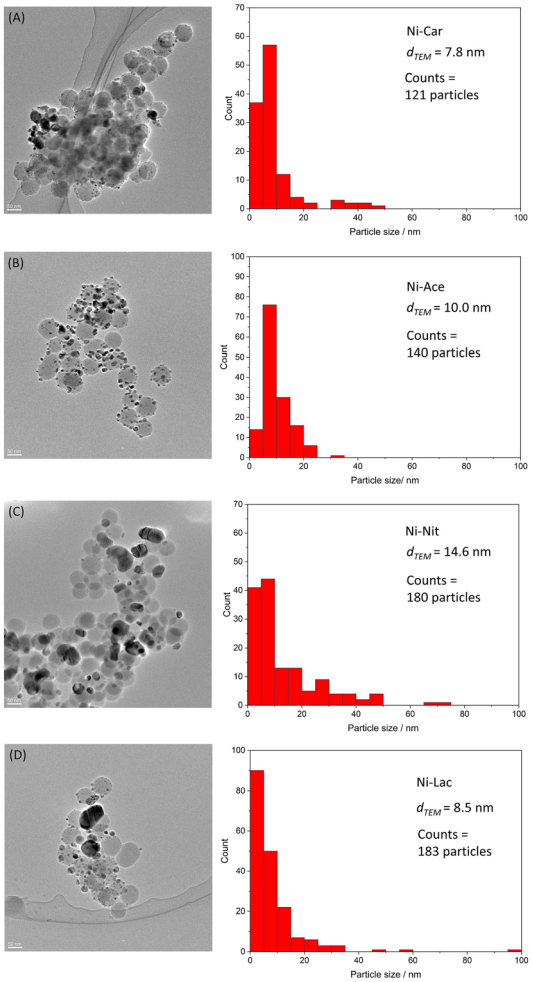

Fig. 2 TEM images and particle size distributions of the Ni/SiO_2 samples after the reduction at 873 K. (A) Ni-Car, (B) Ni-Ace, (C) Ni-Nit, and (D) Ni-Lac.

Table 1 Structural properties of the Ni/SiO_2 samples

Entry	Sample	d_{XRD}[a]/nm	d_{TEM}[b]/nm	D[c] (%)	S_a[d]/m^2 g^{-1}
1	Ni-Car	18.9	7.8	5.5	88.9
2	Ni-Ace	11.0	10.0	9.5	61.0
3	Ni-Nit	24.9	14.6	3.9	61.5
4	Ni-Lac	43.2	8.5	3.1	52.5
5	SiO_2	—	—	—	57.1

[a] Crystallite size calculated from a line width of the Ni(111) peak in the XRD patterns. [b] Mean particle size (number-averaged) of Ni particles estimated from the TEM images. [c] Ni dispersion, [number of surface Ni atoms]/[number of total Ni atoms], calculated from the particle size distributions by TEM (Fig. 2). [d] Specific surface area measured by N_2 adsorption experiments.

Fig. 3 shows the DR UV/vis/NIR spectra of the pristine SiO_2 and reduced Ni/SiO_2 samples at 873 K. The small peaks at wavelengths of 1390, 1900 and 2210 nm were observed in all the samples, which can be assigned to surface hydroxyl groups and adsorbed water.[49] The pristine SiO_2 sample exhibited high diffuse reflectance (>80%), while intense absorption in the visible and near-infrared range (less reflectance <15%, 400–2400 nm) was recorded in all the Ni/SiO_2 samples. These results indicate that the metallic Ni particles function as the light-harvesting sites.[50–52]

Catalytic activity in PTSRM

The time course of the PTSRM reaction was first investigated over the four Ni samples (Fig. S5†) for 120 min. The catalytic activities on Ni-Car, Ni-Ace and Ni-Nit were stable but decreased with time on Ni-Lac. In the Ni-Lac sample, coke formation was not observed by TG-DTA (Fig. S6†). Based on the TEM images (Fig. S7†) and XRD patterns (Fig. S8†), the particle size of Ni increased after the reaction, suggesting that the deactivation in Ni-Lac results from the aggregation of Ni particles. Fig. 4 shows the comparison of the production rates of H_2, CO_2 and CO after 120 min of the reactions. The Ni-Car, Ni-Ace, and Ni-Nit samples showed similar activities, and Ni-Lac showed the lowest one among the samples, where there was no significant difference in the $T_{max,f}$ values between the samples (Fig. 4). Moreover, the CO formation was clearly observed only in the case of Ni-Car (1.2 mmol h^{-1}), while tiny amounts of CO were detected in the other samples (0.1–0.2 mmol h^{-1}). The light to chemical conversion efficiency (eqn (7)) was also plotted in Fig. 4 and the highest value was 2.6% in the Ni-Car sample. Separately, we confirmed that a bare SiO_2 sample did not show activity for PTSRM, which indicates that the Ni particles work as the catalytic active sites.

For comparison, a thermocatalytic steam reforming of methane (TSRM) reaction was performed with an electric heater in the dark (Fig. 5) at 773 and 723 K. In these experiments, the reaction temperatures were set to be comparable to the catalytic activity in PTSRM. At 773 K, the production rates of H_2 and CH_4 conversion were 36–38 mmol h^{-1} and 44–46%, respectively, in all the samples, and there was no significant difference in the activity. The obtained CH_4 conversion was close to the calculated equilibrium conversion (CH_4 conversion = 45.7%) (Table S2†). These catalytic activities reached near equilibrium, which would cause no significant difference in the activity between the samples at 773 K. In contrast, the Ni-Lac sample did not reach equilibrium (CH_4 conversion = 32.2%) at the lower temperature of 723 K, while the other samples reached it.

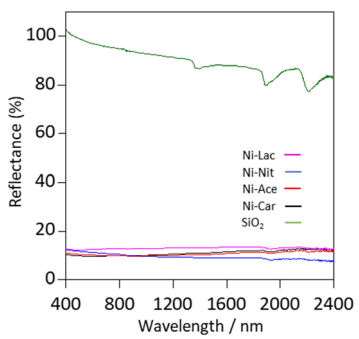

Fig. 3 DR UV/vis/NIR spectra of the Ni/SiO_2 samples after the reduction pretreatment at 873 K.

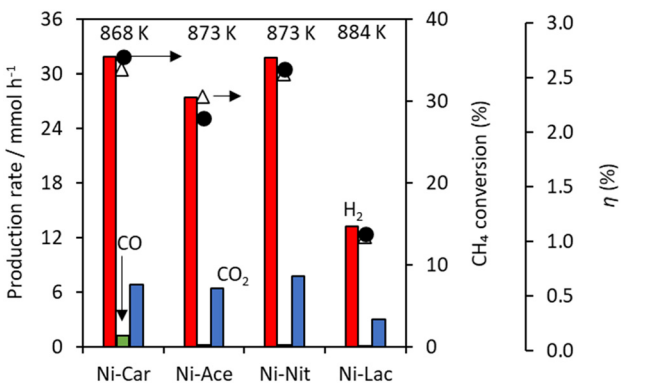

Fig. 4 Production rates of H_2 (red), CO_2 (blue), and CO (green), CH_4 conversions (black circles), and light to chemical conversion efficiencies (η, eqn (7)) (open triangle) in PTSRM over the Ni/SiO_2 samples. The outlet gas was sampled 120 min after starting photoirradiation. The temperatures at the top of the bars were the highest front-side temperatures of the reactor ($T_{max,f}$). Reaction conditions; catalyst weight: 0.5 g, total gas flow rate: 100 ml min^{-1}, reactant gas concentrations: 8% CH_4/12% H_2O/6% N_2/Ar (balance), light power: 23.8 W, wavelength of light: $\lambda > 420$ nm.

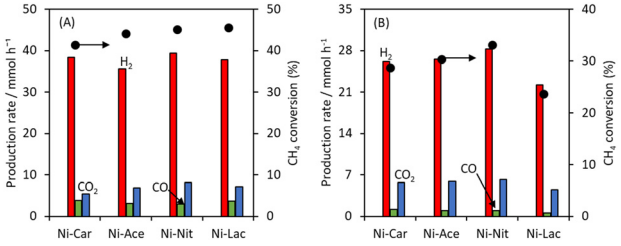

Fig. 5 Production rates of H_2 (red), CO_2 (blue), and CO (green), and CH_4 conversion (black circles) in TSRM over the Ni/SiO_2 samples at (A) 773 K and (B) 723 K. The outlet gas was sampled 60 min after starting the reaction. The catalyst amount, reactant gas concentrations, and total flow rates were the same as those in Fig. 4.

The lower activity of Ni-Lac would be due to the fewest surface Ni sites (*i.e.*, lowest dispersion, Table 1) in TSRM. These results mean that, at high temperatures, thermodynamic constraints dominate the activity, while the kinetic factor also affects the reaction rate at the lower temperature (723 K) under the present conditions of TSRM.

The influence of the light power on the PTSRM activity on the Ni-Car sample was investigated (Fig. 6) by changing the current values of the power supply. No reaction proceeded in the dark (*i.e.*, 0 W), and both the temperature and activity increased with increasing the light power from 8.4 to 23.8 W. In the moderate light powers of 8.4 and 15.8 W, only H_2 and CO_2 were produced, and CO was formed only at the highest light power of 23.8 W. The CO formation is thermodynamically preferable in higher temperature regions,[53,54] which would result in an increased amount of CO at a high light power in PTSRM.

The stability of Ni-Car in the PTSRM reaction was further evaluated for 30 h (Fig. 7) under the same reaction conditions as mentioned in Fig. 4. The production rates of H_2, CO and CO_2 were not changed even after 30 h. The XRD pattern of the used Ni-Car sample confirmed no obvious change in the Ni particle size before and after a long-time reaction (Fig. S9†). Furthermore, 5 cyclic reaction tests (one cycle: 4 h) were performed, where the reduction pretreatment at 873 K was carried out between the cycles. No obvious change in the PTSRM activity was observed (Fig. S10†). These results evidenced the high stability of the Ni-Car sample in the current PTSRM reaction.

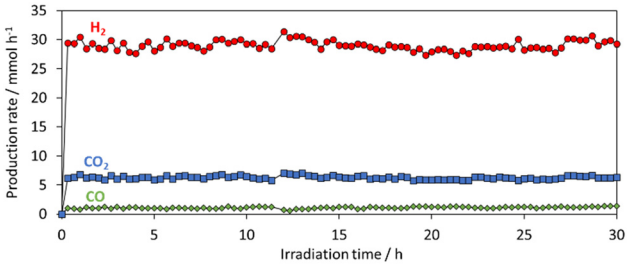

Fig. 7 Long-time reaction test in PTSRM on Ni-Car. The reaction conditions are the same as those mentioned in the caption of Fig. 4.

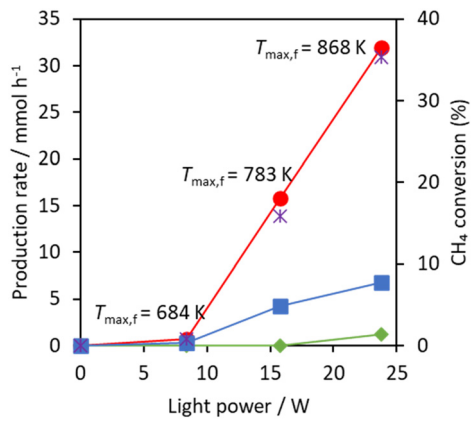

Fig. 6 Production rates of H_2 (circles), CO_2 (squares), and CO (diamonds), and CH_4 conversion (asterisk) at various light powers. Catalyst: Ni-Car. The reaction conditions are the same as those mentioned in the caption of Fig. 4.

The spot size of the concentrated light changes the intensity of light. To investigate the effect of the spot size on the catalytic performance, we performed PTSRM on the Ni-Car sample with various spot sizes, where the spot size was controlled by changing the distance between the reactor and the light source. By decreasing the spot diameter from 2.0 cm to 1.4 cm (Fig. 8A), the H_2 production rate and CH_4 conversion increased (Fig. 8B). At the smallest spot size of 1.4 cm, the CH_4 conversion was 46.0%, and the light-to-chemical conversion efficiency was calculated to be 3.1% based on eqn (7). Then, we measured the surface temperatures of the irradiated side of the reactor at the spot size of 2.0 cm in PTSRM on Ni-Car (*i.e.*, the same conditions as those in Fig. 4) as shown in Fig. 8A. In these measurements, the two-dimensional temperature image was measured by changing the temperature measurement positions for the IR thermometer. The surface temperature concentrically decreased with the highest temperature at the center. Next, we measured the surface temperatures at different measurement positions moved vertically below the maximum temperature point (Fig. 8A) at various light spot sizes (Ø = 2.0–1.4 cm). The temperature decreased by moving the measurement point to the lower side at all the spot sizes (Fig. 8C). With increasing the spot size, $T_{max,f}$ tended to monotonically decrease (Fig. 8D, *i.e.*, 0 mm in Fig. 8C), while the surface temperature at 8 mm below ($T_{8mm,f}$) had a minimum value. Note that the largest light spot in the current study (2.0 cm) was inscribed in a square reactor (Fig. 8A), and in the smaller spot sizes (<2.0 cm), the outer part of the light spot is not directly heated by light. Thus, the different trends could be explained by the balance of the heat generation by light and heat transfer from the centre side of the light spot. More importantly, the temperature gradient on the irradiated reactor surface becomes larger in smaller spot sizes (Fig. 8C). In addition, $T_{max,b}$ also decreased monotonically with increasing the spot size (Fig. 8D), and the difference between $T_{max,f}$ and $T_{max,b}$ increased by decreasing the spot size, possibly due to the higher heat transfer in the

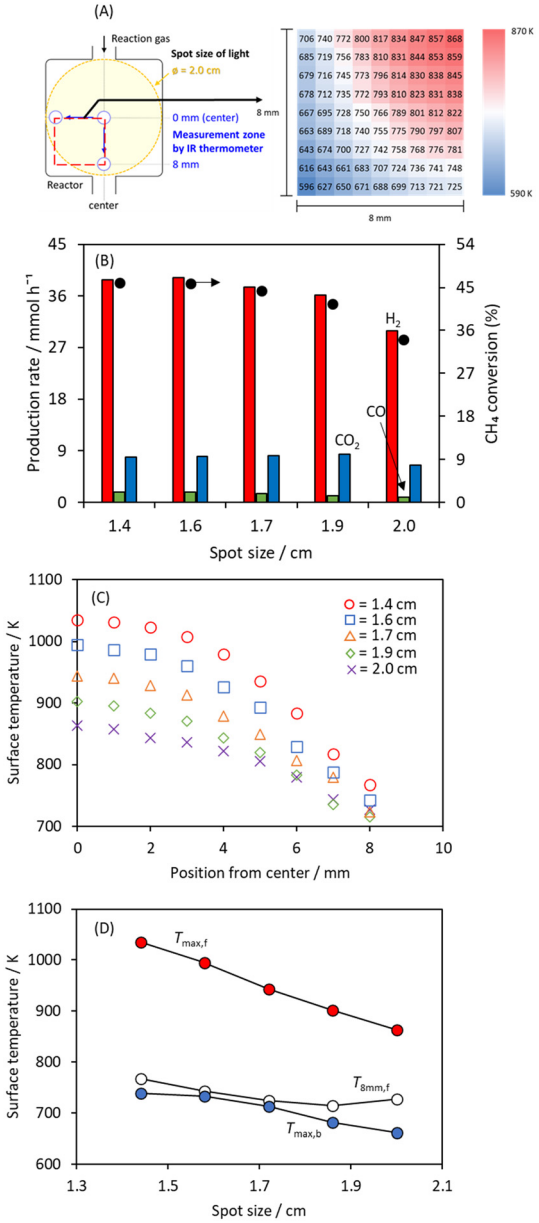

Fig. 8 (A) Schematic illustration for the temperature measurements and a 2-dimensional temperature image of the reactor in PTSRM on Ni-Car. The reaction conditions are the same as those in Fig. 4. (B) Production rates of H_2 (red), CO_2 (blue), and CO (green), and CH_4 conversion (black circles) in PTSRM on Ni-Car in various spot sizes of light (Ø = 2.0–1.4 cm). The product was sampled 60 min after starting photoirradiation. (C) Surface temperatures of the reactor at different measurement positions at various spot sizes. The horizontal axis is the distance between the points of the maximum temperature. (D) Surface temperatures of the reactor at different positions. Red: $T_{max,f}$, blue: $T_{max,b}$, and white: temperature at the point below 8 mm from the maximum temperature point ($T_{8mm,f}$).

larger temperature difference. Thus, the temperature gradient was formed under all the spot size conditions and became larger using the smaller spot size in both horizontal (from the front to the back) and vertical (from the centre to below) directions to light irradiation. The PTSRM activity increased by decreasing the spot size to 1.7 cm, which would be due to the temperature increase derived from the high light intensity. But, surprisingly, the PTSRM activity became stable at less than 1.7 cm despite the significant increase of $T_{max,f}$. This trend could be explained by the reverse reaction of eqn (1) and (3) at the lower temperature zone below the centre of the light spot with the maximum temperature; even though a high conversion is obtained upstream at the high-temperature zone, the reverse reaction could proceed downstream up to the thermodynamic equilibrium under that low-temperature condition.

Comparison between PTSRM and TSRM

At Ø = 2.0 cm, the CH_4 conversion in PTSRM was 34.1% (Fig. 4, $T_{max,f}$ = 868 K), which was lower than that in TSRM at 773 K (44.0%, Fig. 5A). In PTSRM, the surface temperature of the reactor decreased by moving away from the centre of the light spot by *ca.* 140 K (Fig. 8C), which indicates that the low-temperature zone in the reactor would cause lower catalytic activity in PTSRM compared to TSRM. The reverse reaction of eqn (1) and (3) (*i.e.*, CO hydrogenation and Sabatier reaction) would proceed at the lower temperature zone downstream of the highest temperature point because it is thermodynamically favourable and can proceed at around 523–823 K on Ni catalysts.[55–58] Moreover, the Ni-Lac sample showed a lower catalytic activity than the other Ni samples in PTSRM despite similar $T_{max,f}$ values (868–884 K, Fig. 4). Based on the contribution of the kinetic factor to the reaction rate in TSRM at the low temperature of 723 K (Fig. 5B), the low PTSRM activity on Ni-Lac would be due to the lowest Ni dispersion among the Ni/SiO_2 samples (Table 1).

The conversion–selectivity relationship (Fig. 9) provided evidence of side reactions in the lower temperature zone in PTSRM. Here, we plotted the CO_2 selectivity (eqn (6)) against the CH_4 conversion with different spot sizes. In TSRM at various temperatures, CO_2 selectivity was almost on the line of the

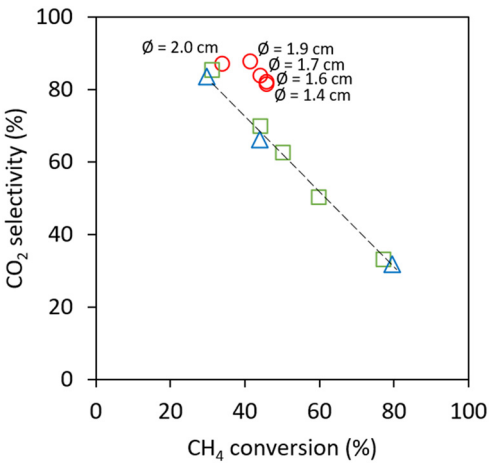

Fig. 9 Relationship between the CH_4 conversion and CO_2 selectivity in PTSRM on the Ni-Car sample. Circles: PTSRM in various spot sizes; triangles: TSRM; squares: equilibrium.

calculated results of the thermodynamic equilibrium. But, in the 2.0 cm spot size, the CO_2 selectivity of PTSRM was 87.3%, which is slightly higher than the line of the equilibrium. Moreover, the smaller spot sizes (*i.e.*, $Ø < 2.0$ cm) at the high conversion ranges showed higher CO_2 selectivity than the results of activity tests in TSRM and thermodynamic calculations. The high CO_2 selectivity suggests that the WGS reaction (eqn (2)) and CO hydrogenation (reverse reaction of eqn (1)) occurred because these reactions increase CO_2 gas or decrease CO gas. It is known that both reactions are favourable thermodynamically at lower temperatures[55,59,60] and can proceed at lower temperatures (573–673 K)[55,61,62] on Ni/SiO_2 compared to SRM (eqn (1)).[7,8] To confirm the effect, we performed the thermal WGS and CO hydrogenation reactions on the Ni-Car sample (Fig. S11 and S12†) using conventional heating, and both reactions occurred at a low temperature of 573 K. Consequently, it is reasonable that the WGS reaction and/or CO hydrogenation in the lower temperature zone downstream (Fig. 8C) contribute to the increased CO_2 selectivity in PTSRM. On the Ni/SiO_2 samples other than Ni-Car, the CO_2 selectivity in PTSRM at $Ø = 2.0$ cm was close to 100% (Ni-Ace: 97.4%, Ni-Nit: 97.8%, and Ni-Lac: 97.5%; after 120 min), which was much higher than that on Ni-Car (87.3%). In the thermal WGS and CO hydrogenation reactions at 573 K, Ni-Car showed the highest activity for WGS but showed a lower activity than Ni-Ace and Ni-Nit for CO hydrogenation (Fig. S11 and S12†). Thus, it is reasonable that CO was formed only on Ni-Car in PTSRM (Fig. 4) because of the low CO consumption rate on Ni-Car by CO hydrogenation at the lower temperature zone below the center of the reactor. Note that the Ni-Lac sample showed a lower CO hydrogenation rate than Ni-Car, but it has also lower activity for PTSRM. This might explain the no CO production on Ni-Lac in PTSRM. Furthermore, we separately confirmed that the WGS reaction is promoted by light irradiation under photothermal conditions at various light intensities (Fig. S13†). Based on these results, the obtained insight shows that the product selectivity is controllable outside the steady-state thermodynamic values using the temperature gradient created by light in a single reactor system.

Conclusions

We investigated the catalytic activity in PTSRM on four 20 wt% Ni/SiO_2 catalysts with different sizes and morphologies of Ni particles, which were prepared by the decomposition of Ni PSs and the impregnation method using different Ni precursors. In TSRM at 773 K in the dark, the CH_4 conversion reached near-equilibrium in all the catalysts, meaning that the prepared catalysts have a sufficient reaction rate under dark conditions to reach the thermodynamic equilibrium at that temperature. Under light irradiation (23.8 W), there was no significant difference in the PTSRM activity for the Ni-Car, Ni-Nit, and Ni-Ace samples, while Ni-Lac showed the lowest activity due to the low Ni dispersion. Moreover, the power and spot size of light affected the reaction rate of PTSRM; as a result, higher $T_{max,f}$ contributed to the higher reaction rate in PTSRM. We found that the CO_2 selectivity in PTSRM was affected by both WGS and CO hydrogenation in the low temperature zone and exceeded the values of experimental TSRM governed by thermodynamics. Based on these results of the activity test and temperature measurement, we concluded that the significant temperature gradient (>240 K, $Ø = 1.4$ cm) formed by concentrated light irradiation is the origin of the characteristic selectivity that cannot be explained by steady-state thermodynamics. This work shows the possibility of controlling the product selectivity by photo-formed temperature gradients for solar energy conversion to chemical energy.

Author contributions

Wirya Sarwana: conceptualization, investigation, and writing – original draft. Daichi Takami: investigation. Akira Yamamoto: conceptualization, funding acquisition, project administration, supervision, and writing – review & editing. Hisao Yoshida: funding acquisition, supervision, and writing – review & editing.

Conflicts of interest

There are no conflicts to declare.

Acknowledgements

This work was financially supported by the Scientific Research (B) (21H01975) and the Fostering Joint International Research (B) (20KK0116) from the Japan Society for the Promotion of Science. W. Sarwana is grateful to the Indonesia Endowment Fund for Education (LPDP), Ministry of Finance Indonesia Republic for financial support during the study. The XAFS experiments were performed under the approval of the Photon Factory Program Advisory Committee (Proposal No. 2020G667). The authors thank Mr. Kiyomura for the TEM observations, supported by the Kyoto University Nano Technology Hub, Kyoto, Japan, under the Nanotechnology Platform Project.

Notes and references

1 S. Uemiya, N. Sato, H. Ando, T. Matsuda and E. Kikuchi, *Appl. Catal.*, 1990, **67**, 223–230.
2 E. Kikuchi, *Catal. Today*, 2000, **56**, 97–101.
3 J. Tong, Y. Matsumura, H. Suda and K. Haraya, *Ind. Eng. Chem. Res.*, 2005, **44**, 1454–1465.
4 C. S. Martavaltzi, E. P. Pampaka, E. S. Korkakaki and A. A. Lemonidou, *Energy Fuels*, 2010, **24**, 2589–2595.
5 X. Zhu, H. Wang, Y. Wei, K. Li and X. Cheng, *J. Rare Earths*, 2010, **28**, 907–913.
6 M. Dan, M. Mihet and M. D. Lazar, *Int. J. Hydrogen Energy*, 2020, **45**, 26254–26264.
7 J. R. Rostrup-Nielsen, L. J. Christiansen and J.-H. Bak Hansen, *Appl. Catal.*, 1988, **43**, 287–303.
8 Y. Matsumura and T. Nakamori, *Appl. Catal., A*, 2004, **258**, 107–114.

9 F. Che, J. T. Gray, S. Ha and J.-S. McEwen, *ACS Catal.*, 2017, **7**, 551–562.
10 H. Song, X. Meng, Z. Wang, H. Liu and J. Ye, *Joule*, 2019, **3**, 1606–1636.
11 A. Giaconia, M. de Falco, G. Caputo, R. Grena, P. Tarquini and L. Marrelli, *AIChE J.*, 2008, **54**, 1932–1944.
12 M. Tutar, C. E. Üstün, J. M. Campillo-Robles, R. Fuente, S. Cibrián, I. Arzua, A. Fernández and G. A. López, *Comput. Chem. Eng.*, 2021, **155**, 107504.
13 R. D. Skocypec, R. E. Hogan and J. F. Muir, *Sol. Energy*, 1994, **52**, 479–490.
14 T. Shimizu, K. Shimizu, Y. Kitayama and T. Kodama, *Sol. Energy*, 2001, **71**, 315–324.
15 A. Berman, R. K. Karn and M. Epstein, *Green Chem.*, 2007, **9**, 626–631.
16 H. B. Do, J. T. Jang and G. Y. Han, *J. Sol. Energy Eng.*, 2012, **134**, 1–4.
17 T. Li, L. Tan, Y. Zhao and Y.-F. Song, *Chem. Eng. Sci.*, 2021, **245**, 116839.
18 P. Wang, X. Zhang, R. Shi, J. Zhao, Z. Yuan and T. Zhang, *Energy Fuels*, 2022, **36**, 11627–11635.
19 H. Yoshida, S. Kato, K. Hirao, J. Nishimoto and T. Hattori, *Chem. Lett.*, 2007, **36**, 430–431.
20 H. Yoshida, K. Hirao, J. Nishimoto, K. Shimura, S. Kato, H. Itoh and T. Hattori, *J. Phys. Chem. C*, 2008, **112**, 5542–5551.
21 K. Shimura, S. Kato, T. Yoshida, H. Itoh, T. Hattori and H. Yoshida, *J. Phys. Chem. C*, 2010, **114**, 3493–3503.
22 K. Shimura and H. Yoshida, *Energy Environ. Sci.*, 2010, **3**, 615–617.
23 K. Shimura, H. Kawai, T. Yoshida and H. Yoshida, *ACS Catal.*, 2012, **2**, 2126–2134.
24 A. Yamamoto, S. Mizuba, Y. Saeki and H. Yoshida, *Appl. Catal., A*, 2016, **521**, 125–132.
25 H. Song, X. Meng, Z. Wang, Z. Wang, H. Chen, Y. Weng, F. Ichihara, M. Oshikiri, T. Kako and J. Ye, *ACS Catal.*, 2018, **8**, 7556–7565.
26 H. Yoshida, S. Mizuba and A. Yamamoto, *Catal. Today*, 2019, **334**, 30–36.
27 B. V. Ayodele, A. A. Ghazali, M. Y. Mohd Yassin and S. Abdullah, *Int. J. Hydrogen Energy*, 2019, **44**, 20700–20710.
28 B. Tan, Y. Ye, Z. Huang, L. Ye, M. Ma and Y. Zhou, *Chin. Chem. Lett.*, 2020, **31**, 1530–1534.
29 A. Anzai, K. Fujiwara, A. Yamamoto and H. Yoshida, *Catal. Today*, 2020, **352**, 1–9.
30 T. Kujirai, A. Yamaguchi, T. Fujita, H. Abe and M. Miyauchi, *Chem. Commun.*, 2021, **57**, 8007–8010.
31 W. Sarwana, A. Anzai, D. Takami, A. Yamamoto and H. Yoshida, *Catal. Sci. Technol.*, 2021, **11**, 5534–5542.
32 W. Sarwana, A. Yamamoto and H. Yoshida, *Catal. Today*, 2022, DOI: **10.1016/j.cattod.2022.07.026**.
33 B. Han, W. Wei, M. Li, K. Sun and Y. H. Hu, *Chem. Commun.*, 2019, **55**, 7816–7819.
34 A. O. Govorov and H. H. Richardson, *Nano Today*, 2007, **2**, 30–38.
35 H. Huang, M. Mao, Q. Zhang, Y. Li, J. Bai, Y. Yang, M. Zeng and X. Zhao, *Adv. Energy Mater.*, 2018, **8**, 1702472.
36 D. Mateo, J. Luis Cerrillo, S. Durini and J. Gascon, *Chem. Soc. Rev.*, 2021, **50**, 2173–2210.
37 A. Loaiza-Gil, M. Villarroel, J. F. Balbuena, M. A. Lacruz and S. Gonzalez-Cortés, *J. Mol. Catal. A: Chem.*, 2008, **281**, 207–213.
38 A. J. Majewski, J. Wood and W. Bujalski, *Int. J. Hydrogen Energy*, 2013, **38**, 14531–14541.
39 C. Suo, Y. Liu, X. Zhang, H. Wang, B. Chen, J. Fang, Z. Zhang, R. Chen, R. Chen and C. Shi, *Eur. J. Inorg. Chem.*, 2022, **2022**, e202200182.
40 C. Mao, H. Li, H. Gu, J. Wang, Y. Zou, G. Qi, J. Xu, F. Deng, W. Shen, J. Li, S. Liu, J. Zhao and L. Zhang, *Chem*, 2019, **5**, 2702–2717.
41 X. Li, X. Zhang, H. O. Everitt and J. Liu, *Nano Lett.*, 2019, **19**, 1706–1711.
42 C. Zhang, H. Yue, Z. Huang, S. Li, G. Wu, X. Ma and J. Gong, *ACS Sustainable Chem. Eng.*, 2013, **1**, 161–173.
43 M. Yang, P. Jin, Y. Fan, C. Huang, N. Zhang, W. Weng, M. Chen and H. Wan, *Catal. Sci. Technol.*, 2015, **5**, 5095–5099.
44 R.-P. Ye, W. Gong, Z. Sun, Q. Sheng, X. Shi, T. Wang, Y. Yao, J. J. Razink, L. Lin, Z. Zhou, H. Adidharma, J. Tang, M. Fan and Y.-G. Yao, *Energy*, 2019, **188**, 116059.
45 H. Du, X. Ma, M. Jiang, P. Yan, Y. Zhao and Z. Conrad Zhang, *Catal. Today*, 2021, **365**, 265–273.
46 M. Mao, Q. Zhang, Y. Yang, Y. Li, H. Huang, Z. Jiang, Q. Hu and X. Zhao, *Green Chem.*, 2018, **20**, 2857–2869.
47 S. Gordon and B. J. Mcbride, Computer Program for Calculation of Complex Chemical Equilibrium Compositions and Applications, *NASA Reference Publication 1311*, 1994.
48 R. J. Matyi, L. H. Schwartz and J. B. Butt, *Catal. Rev.: Sci. Eng.*, 1987, **29**, 41–99.
49 M. Takeuchi, G. Martra, S. Coluccia and M. Anpo, *J. Phys. Chem. B*, 2005, **109**, 7387–7391.
50 S. M. Williams, A. D. Stafford, K. R. Rodriguez, T. M. Rogers and J. V. Coe, *J. Phys. Chem. B*, 2003, **107**, 11871–11879.
51 D. A. Perry, R. L. Borchers, J. W. Golden, A. R. Owen, A. S. Price, W. A. Henry, F. Watanabe and A. S. Biris, *J. Phys. Chem. Lett.*, 2013, **4**, 3945–3949.
52 D. Takami, Y. Ito, S. Kawaharasaki, A. Yamamoto and H. Yoshida, *Sustainable Energy Fuels*, 2019, **3**, 2968–2971.
53 M. A. Rosen, *Int. J. Hydrogen Energy*, 1991, **16**, 207–217.
54 A. E. Lutz, R. W. Bradshaw, J. O. Keller and D. E. Witmer, *Int. J. Hydrogen Energy*, 2003, **28**, 159–167.
55 C. H. Bartholomew, R. B. Pannell and J. L. Butler, *J. Catal.*, 1980, **65**, 335–347.
56 L. Xu, F. Wang, M. Chen, D. Nie, X. Lian, Z. Lu, H. Chen, K. Zhang and P. Ge, *Int. J. Hydrogen Energy*, 2017, **42**, 15523–15539.
57 D. Takami, A. Yamamoto and H. Yoshida, *Catal. Sci. Technol.*, 2020, **10**, 5811–5814.
58 Y. Chen, W. Bi, L. Chen and Q. Liu, *Int. J. Hydrogen Energy*, 2021, **46**, 27567–27575.
59 S. Z. Ozdogan, P. D. Gochis and J. L. Falconer, *J. Catal.*, 1983, **83**, 257–266.
60 X. Cao, Y.-F. Han, C. Peng and M. Zhu, *ChemCatChem*, 2022, **14**, e202200190.
61 J. Ashok, M. L. Ang, P. Z. L. Terence and S. Kawi, *ChemCatChem*, 2016, **8**, 1308–1318.
62 P. Liu, B. Zhao, S. Li, H. Shi, M. Ma, J. Lu, F. Yang, X. Deng, X. Jia, X. Ma and X. Yan, *Ind. Eng. Chem. Res.*, 2020, **59**, 1845–1854.